RESEARCH ARTICLE

A novel geometrical design of gas-to-gas planar membrane humidifier for proton electrolyte membrane fuel cells

Bing-Bing Wang[1] | Wen-Ken Li[2] | Chung-Yuan Lee[3,4] | Wei-Mon Yan[3,4] |
Mohammad Ghalambaz[5,6]

[1]School of Energy and Power Engineering, Northeast Electric Power University, Jilin, China

[2]Department of Mechanical Engineering, Chung Yuan Christian University, Taoyuan, Taiwan

[3]Department of Energy and Refrigerating Air-Conditioning Engineering, National Taipei University of Technology, Taipei, Taiwan

[4]Research Center of Energy Conservation for New Generation of Residential, Commercial, and Industrial Sectors, National Taipei University of Technology, Taipei, Taiwan

[5]Metamaterials for Mechanical, Biomechanical and Multiphysical Applications Research Group, Ton Duc Thang University, Ho Chi Minh City, Vietnam

[6]Faculty of Applied Sciences, Ton Duc Thang University, Ho Chi Minh City, Vietnam

Correspondence
Wei-Mon Yan, Department of Energy and Refrigerating Air-Conditioning Engineering, National Taipei University of Technology, Taipei 10608, Taiwan.
Email: wmyan@ntut.edu.tw

Mohammad Ghalambaz, Ton Duc Thang University, Ho Chi Minh City, Vietnam.
Email: mohammad.ghalambaz@tdtu.edu.vn

Summary

A gas-to-gas membrane humidifier recovers heat and water from the wet hot exhaust gas of a proton electrolyte membrane fuel cell and keeps the inlet feed air of the cell warm and humid. This type of humidifier does not need external water sources, and it is compact and efficient with practical applications in portable devices and automobiles. In the present study, four potential designs of gas-to-gas planar membrane humidifiers were introduced, and their characteristic behavior was examined. The simulation results showed that the geometrical design of the humidifier channels could notably influence the efficiency of the device. It was found that a three-inlet serpentine humidifier could provide the largest water recovery ratio and the heat transfer rate among the proposed designs, with a slight increase in the pressure drop. Hence, the three-inlet design was selected as the optimal geometrical design of the humidifier. Then, the impacts of design parameters on the characteristic behavior of the three-channel model were explored. The results show an increase in the outlet (wet side) temperature and relative humidity enhances the water recovery and efficiency of the humidifier. The outcomes of the present research are of practical interest for the design of novel commercial humidifiers.

KEYWORDS
energy efficiency, fuel cell water recovery, gas-to-gas planar membrane humidifiers, geometrical design, three-channel membrane humidifier

1 | INTRODUCTION

Providing adequate moisture to a fuel cell and maintaining the humidity inside a stack are crucial tasks, which should be taken into account in the fuel cell designs and applications. The dehydration of the fuel cell and the thin membrane could be avoided by heating and humidifying the gas at the cathode inlet of the fuel cell. The humidification control and its influence on the performance of fuel cells have been highlighted in many recent investigations.[1-3] The literature review shows that there are several practical approaches for providing moisture to the inlet gas. From a general point of view, these approaches can be divided into internal and external humidification methods. The internal approaches are classified as chemical methods and physical methods. The external approaches include enthalpy wheel humidification,[4] direct water injection,[5] gas bubbling humidification,[6,7] exhaust gas recirculation,[8] and membrane humidifiers.[9,10] Some of these approaches have been reviewed in the recent study of Chang et al.[11]

Among the available humidification approaches, the gas-to-gas membrane humidifier is an efficient and practical approach that can efficiently increase the temperature and humidity of the inlet gas in the fuel cell. Thus, the need for an external water supply can be minimal or none. In this approach, the humidity and heat will be recovered from the fuel cell's hot and wet exhaust gas. The dry and cold air, as well as the wet exhaust gas from the fuel cell outlet, are introduced into the humidifier. There is a membrane in the humidifier between the wet and dry streams, which allows heat and moisture transport between the two streams. During the humidification process, the dry and cold gas absorbs moisture and heat from the hot and humid exhaust gas. Then, the heated and humidified gas enters the cathode of the fuel cell stack while the depleted exhaust gas purges to the atmosphere. The humid and heated gas maintains the moisture inside the fuel cell stack and keeps the stack operating at high efficiency.

The gas-to-gas humidifiers do not require an external source for the water supply, and they are light and efficient. Hence, they are a promising solution for the humidification of fuel cells in portable and automobile applications. Nowadays, many recent patents have been filed on the design and apparatus of membrane humidifiers for fuel cell applications,[12-15] and some planar models of these humidifiers have been commercialized.[16] Most of the available literature works have focused on the simple design of gas-to-gas humidifiers and examined their performance through experimental approaches. For example, Chen et al[17] developed a planar membrane humidifier for a proton exchange membrane fuel cell (PEMFC) and tested the influence of the counterflow and parallel flow, the airflow, the humidity, and the temperature of the dry air on the efficiency, water recovery ratio (WRR), dew point approach approximate temperature (DPAT), and pressure drop of the humidifier. The results showed that an increase in airflow rate improves the overall accumulated water, but it does not improve WRR and DPAT. Moreover, at a fixed relative humidity, a rise in the inlet air temperature is not beneficial for WRR.

Yan et al[18] constructed a gas-to-gas membrane humidifier and experimentally investigated the geometrical impact of the channel size of the humidifier on the humidifier behavior. The influence of dry air inlet conditions (temperature and humidity) was also examined. The results showed that the variation of the depth and width of the channel notably alters the humidification efficiency. There are also some theoretical models for simulation of the heat and mass transfer behavior of gas-to-gas membrane humidifiers. For example, Aytabi et al[19] proposed a new design of humidifiers with cross-flow channels, while Solsona et al[20] developed a model for Nafion membrane gas humidifiers based on experimental data for fuel cell applications. Afshari et al[21] introduced theoretical and numerical models for the gas-to-gas membrane humidifiers. They investigated the impact of the membrane area and thickness, and the channel hydraulic diameter on the behavior of planar membrane humidifiers (PMH). Their results showed a reduction in the humidifier efficiency by the growth of the membrane thickness. Moreover, the rise of the membrane area could enhance the humidifier's efficiency. Kong et al[22] employed a substrate to promote the efficiency of a humidifier for fuel cell applications. The outcomes demonstrated that by applying the substrate, the cell efficiency and the recovered water rate were considerably enhanced.

Chen et al[23] experimentally investigated different structures of PMH for water recovery. They also examined parallel and counterflow configurations. The results showed that counterflow configuration could provide the best water recovery. Increasing the depth and width of a channel could increase water recovery. Afshari and Houreh[24] proposed three novel designs for PMH structures involving metal foams. In the first design, they used a uniform metal foam for the dry side channel, while the wet side was made of regular straight channels. In the second design, the wet side was made of metal foam, while the dry side was made of regular straight channels. In the third design, both of the wet side and dry side channels were made of metal foams. It was found that placing a metal foam at dry side cannot positively improve the water recovery, but placing the metal foam at wet side and both sides could improve the water recovery for PMH.

The literature review indicates that the humidifier efficiency and water recovered ratio depend on the

geometrical design of the humidifier channels. Hence, a well-designed humidifier could notably improve the amount of the recovered water, and consequently, the performance of the fuel cell stack is optimized. In our recent publications,[25,26] a mathematical model was introduced based on computational fluid dynamics for PMH simulation with gas-to-gas membranes. The model was tested and validated against the literature data, and an excellent agreement was found. Then, the proposed model was employed to study the conventional direct gas-to-gas membrane humidifiers.

Yan et al[25] utilized the conventional direct gas-to-gas membrane humidifiers, and they examined the influence of various control parameters such as the inlet temperature and mass flow rates on the heat and mass transfer behavior of the PMH. Later, Yan et al[26] surveyed the effect of the aspect ratio (AR) of the flow passage channels (width/height) and channel lengths on the PMH's pressure drop, WRR, and coefficient of performance (COP). The results showed that an increase in the AR improves the heat and mass transfer as well as COP. The main reason for the enhanced performance was the larger membrane surface between the two flows. Thus, the geometrical design of PMH's plays a crucial role in the heat and mass transfer behavior and efficiency of this type of humidifier.

Although using a large AR led to an extensive membrane surface, the mechanical failure of the membrane and the increased size of the humidifier were the main drawbacks of the proposed humidifier design.

Since the PMH's geometrical design shows a notable influence on the heat and mass transfer behavior and efficiency of these humidifiers, exploring new fundamental designs is a crucial task, which should be persuaded in future researches. The present study aims to explore the advantage of adopting serpentine channels for a gas-to-gas PMH in PEM fuel cell for the first time. Considering a constant volume of gas-to-gas PMH, the serpentine channels could provide a potential long contact passage between the cold and dry sides through the membrane and thus lead to a better heat and mass transfer performance.

2 | MATHEMATICAL MODEL

2.1 | The humidifier model

A schematic view of the physical model of gas-to-gas PMH is depicted in Figure 1. The cold atmospheric dry air enters the humidifier from one side, and the hot and wet air at the exhaust (outlet) of the fuel cell enters from the opposite
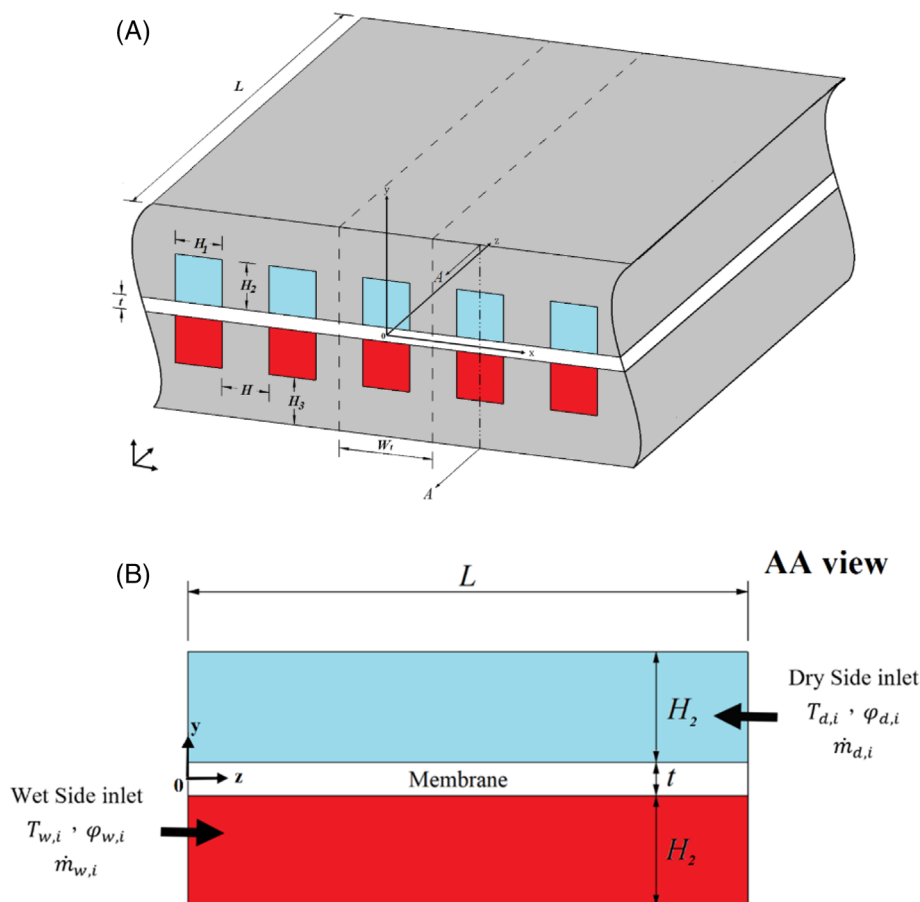
FIGURE 1 Physical model of the gas-to-gas PMH [Colour figure can be viewed at wileyonlinelibrary.com]

(A)

(B)

(C)

(D)

(E)
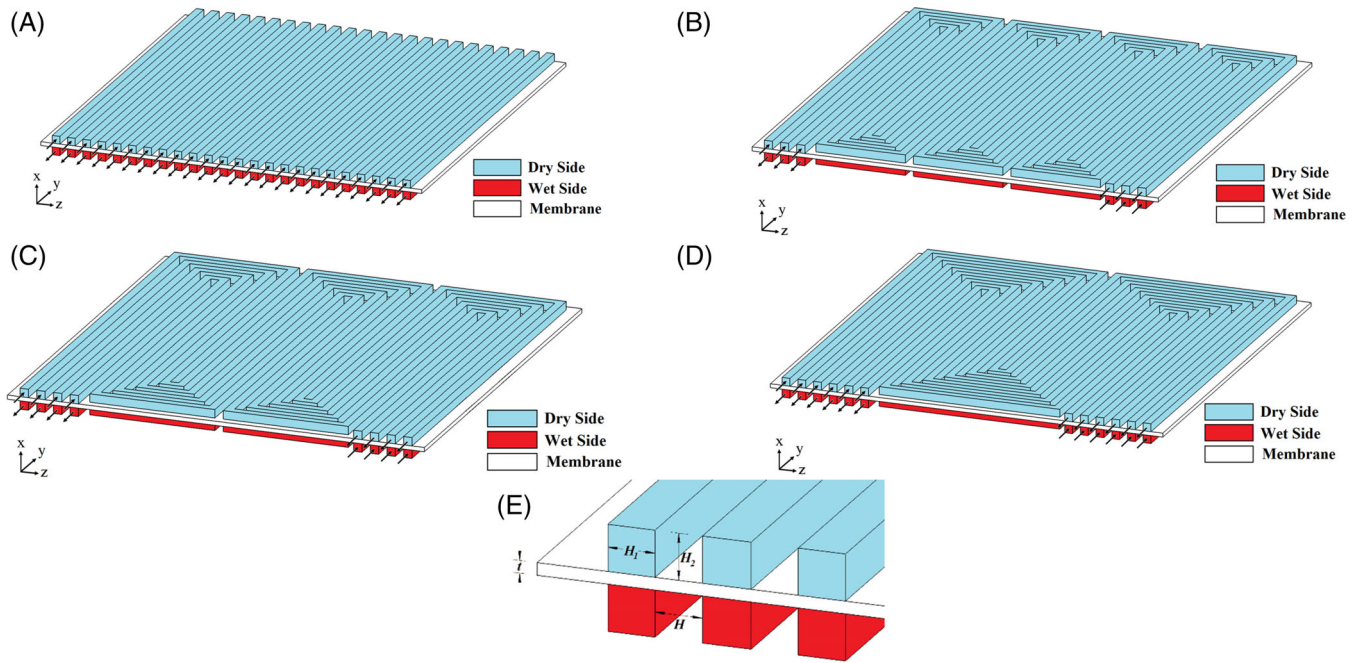
FIGURE 2 Geometrical appearance of each flow channel. (A) Straight flow channel, (B) three-serpentine flow channel, (C) four-serpentine flow channel, (D) six-serpentine flow channel, and (E) flow path size symbol [Colour figure can be viewed at wileyonlinelibrary.com]

side. There is a porous membrane layer, which separates the two flow streams and allows heat and mass transfer between them. In the humidifier, the fresh atmospheric air gets warm due to the heat transfer with the hot exhaust gas, and its capability to hold moisture increases. The wet exhaust air in the opposite direction loses some of its heat to the cold flow, and its capacity to carry water vapor reduces. Thus, the water vapor transfer (mass transfer) from the wet-side to the dry-side occurs through the membrane. In Figure 1B, T, φ, and $\dot{m}$ denote the temperature, the relative humidity, and the mass flow rate of the flow streams, respectively. The subscripts of w, and d denote the wet and dry sides while i indicates the inlet sides of the channels. As seen in Figure 1A, t is the membrane thickness, H is the flow channel spacing, H_1 is the flow channel width, and H_2 is the flow channel height.

Figure 2 illustrates the geometric appearance of each flow channel for straight-through (Figure 2A) three-serpentine (Figure 2B), four-serpentine (Figure 2C), and six-serpentine (Figure 2D) flow channels. The dimension of each of the humidifiers is 50 mm × 50 mm × 4.025 mm. The number of flow channels is 24 in the straight flow channel without turns, while the number of turns of the three-serpentine, four-serpentine, and six serpentine flow channels is seven, five, and three, respectively. The geometrical characteristics of the channel cross-sections are depicted in Figure 2E, and their magnitudes are reported in Table 1.[9,17,18]

2.2 | Governing equations

The governing equations for PMH consist of the continuity of the air mixture, the momentum of the air mixture in channels and porous membrane, the concentration equation for vapor phase, and the energy equations in the channels and the membrane. The following assumptions were considered in the modeling of PMH. The flow is steady-state, incompressible, and laminar, and the ideal gas mixtures can model the mixture behavior. There is a local thermal equilibrium between the membrane and the mixture. The air diffusion across the membrane was neglected, and the membrane is homogeneous and isotropic; thus, it has a constant porosity and permeability. The thermophysical properties are assumed to be constant in order to simplify the analysis. The governing equations in the form of partial differential equations are introduced as[9,24,26]:

The continuity equation for the mixture.

$$\frac{\partial u}{\partial x} + \frac{\partial v}{\partial y} + \frac{\partial w}{\partial z} = 0 \tag{1}$$

where u, v, and w indicate the components of the mixture velocity in x, y, and z directions, respectively. Since the density is assumed constant (incompressible flow), the density variations were removed from the continuity equation.

TABLE 1 The geometrical and thermophysical specifications of the humidifier[9,17,18]

Input parameters	Values
Channel width	2 mm
Channel length	200 mm
Membrane thickness	25 μm
Flow channel height or width	1 mm
Inlet temperature at the wet side	80°C
Inlet temperature at the dry side	30°C
Inlet mass flow rate at the wet side	$4.5\text{-}18 \times 10^{-6}$ kg/s
Inlet mass flow rate at the dry side	$4.5\text{–}18 \times 10^{-6}$ kg/s
Inlet relative humidity at the wet side	100%
Inlet relative humidity at the dry side	0%
Diffusivity of air vapor at standard state	1.641×10^{-5} m²/s
Universal gas constant	0.2891 J/kg K
Air-water vapor mixture viscosity	1.72×10^{-5} Pa s
Operating pressure	151.987 kPa
Weight of dry membrane	1 kg/kmol
Density of dry membrane	1000 kg/m³
Permeability of membrane	10^{-12} m²
Porosity of membrane	0.5
Thermal conductivity of Nafion membrane	0.95 W/m K
Thermal conductivity air-vapor	0.0454 W/m K

The momentum equations in x, y, and z directions for the mixture.

$$\frac{\rho}{\varepsilon^2}\left[u\frac{\partial u}{\partial x}+v\frac{\partial u}{\partial y}+w\frac{\partial u}{\partial z}\right]=-\frac{\partial p}{\partial x}+\mu\left[\frac{\partial^2 u}{\partial x^2}+\frac{\partial^2 u}{\partial y^2}+\frac{\partial^2 u}{\partial z^2}\right]+S_u \quad (2)$$

$$\frac{\rho}{\varepsilon^2}\left[u\frac{\partial v}{\partial x}+v\frac{\partial v}{\partial y}+w\frac{\partial v}{\partial z}\right]=-\frac{\partial p}{\partial y}+\mu\left[\frac{\partial^2 v}{\partial x^2}+\frac{\partial^2 v}{\partial y^2}+\frac{\partial^2 v}{\partial z^2}\right]+S_v \quad (3)$$

$$\frac{\rho}{\varepsilon^2}\left[u\frac{\partial w}{\partial x}+v\frac{\partial w}{\partial y}+w\frac{\partial w}{\partial z}\right]=-\frac{\partial p}{\partial z}+\mu\left[\frac{\partial^2 w}{\partial x^2}+\frac{\partial^2 w}{\partial y^2}+\frac{\partial^2 w}{\partial z^2}\right]+S_w \quad (4)$$

Here, p indicates the pressure field, and S_u, S_v, and S_w represent the Darcy law source terms in the porous membrane, and they will be introduced later. The symbols of ρ, μ, and ε denote the density of the mixture, the dynamic viscosity of the mixture, and the porosity of the membrane, respectively. The Darcy source terms are incorporated as[27]:

$$S_u=-\frac{\mu}{K}u, \quad S_v=-\frac{\mu}{K}v, \quad S_w=-\frac{\mu}{K}w \quad (5)$$

where K is the permeability of the membrane. In the case of clear flow in the channel, the porosity is unity and the permeability is a very large number, which forces the Darcy source terms to zero. This way, the conventional Navier and Stokes equations will be recovered in the channels.

The concentration equation for the vapor phase

$$\left[u\frac{\partial C}{\partial x}+v\frac{\partial C}{\partial y}+w\frac{\partial C}{\partial z}\right]=D^{\text{eff}}\left[\frac{\partial^2 C}{\partial x^2}+\frac{\partial^2 C}{\partial y^2}+\frac{\partial^2 C}{\partial z^2}\right] \quad (6)$$

In which, C represents the total concentration vapor, and D^{eff} shows the effective diffusivity of the vapor in the air. The effective diffusivity in the porous membrane with a porosity of ε was computed using the Bruggeman correction[25,28]:

$$D^{\text{eff}}=\varepsilon^{1.5}D \quad (7)$$

The following state equation was employed to compute the vapor diffusivity, D, using the temperature and pressure[26]:

$$D=D_0\left(\frac{T}{T_0}\right)^{1.5}\left(\frac{p}{p_0}\right) \quad (8)$$

Here, the standard temperature and pressure of $T_0 = 273.15$ K and $p_0 = 101.3$ kPa were used as reference. Besides, D_0 exhibits the standard diffusivity coefficient. The following relation was applied to evaluate the vapor diffusivity[26,29]:

$$D_m^{\text{H}_2\text{O}}=\begin{cases} 3.1\times 10^{-7}\lambda\left(e^{0.28\lambda}-1\right).e^{(-2346/T)} & \text{for } 0<\lambda\leq 3 \\ 4.17\times 10^{-8}\lambda\left(1+161e^{-\lambda}\right).e^{(-2346/T)} & \text{otherwise} \end{cases} \quad (9)$$

where λ denotes the moisture in the membrane and computed as follow[25,30]:

$$\lambda=\begin{cases} 0.043+17.81a-39.85a^2+36a^3 & \text{for } 0<a\leq 1 \\ 14+1.4(a-1) & \text{for } 1<a\leq 3 \\ 16.8 & \text{for } a>3 \end{cases} \quad (10)$$

in which a is the vapor activity and can be computed as:

$$a=\frac{C^{\text{H}_2\text{O}}RT}{p_{\text{sat}}} \quad (11)$$

The membrane's moisture was computed using the following relation[25,26]:

$$C_m^{H_2O} = \frac{\lambda \rho_{m,dry}}{W_{m,dry}} \qquad (12)$$

where $\rho_{m,dry}$ and $W_{m,dry}$ denote the density and equivalent weight of dry membrane, respectively.

Energy equations for air mixture in channels and membrane under local thermal equilibrium:

$$\rho C_p \left[u\frac{\partial T}{\partial x} + v\frac{\partial T}{\partial y} + w\frac{\partial T}{\partial z} \right] = k_{eff} \left[\frac{\partial^2 T}{\partial x^2} + \frac{\partial^2 T}{\partial y^2} + \frac{\partial^2 T}{\partial z^2} \right] \qquad (13)$$

Here, k_{eff} shows the thermal conductivity of the air mixture inside the channel and membrane, C_p stands for the specific heat capacity of the air mixture. The effective thermal conductivity (k_{eff}) was computed using the porosity of the membrane (ε), the thermal conductivities of the membrane (k_m) and water (k_w)[31]:

$$k_{eff} = \frac{1}{\frac{1-\varepsilon}{3k_m} + \frac{\varepsilon}{2k_m+k_w}} - 2k_m \qquad (14)$$

wherein the case of clear flow in a channel, the porosity is unite and the above equation recovers the thermal conductivity of the air mixture.

Energy equation in the solid walls.

$$k_s \left[\frac{\partial^2 T}{\partial x^2} + \frac{\partial^2 T}{\partial y^2} + \frac{\partial^2 T}{\partial z^2} \right] = 0 \qquad (15)$$

Here, k_s shows the wall's thermal conductivity.[32]

2.3 | Boundary conditions

The no-slip and impermeability of mass are employed at all walls. Following,[25,26] the inlet boundary conditions are the prescribed temperature, humidity, and mass flow rates at the inlets of the channels for the wet and dry sides. The fluid enters the channel uniformly. The outlet boundary conditions are also fully developed outlet flow with no flux. The temperature and energy balance were employed at the wall interfaces.

2.4 | The characteristics parameters

2.4.1 | Dew point approach temperature

The Dew Point Approach Temperature (DPAT) of the humidifier shows the distance between the dry outlet and wet inlet dew point temperatures. In the case of excellent

mass transfer, the dry side outlet will absorb the heat and moisture from the hot wet stream, and hence, the difference between the dew point temperature of the outlet of the dry side and the inlet of the wet side reduces. As a result, the lower DPAT and the better humidifier efficiency are obtained. Here, DPAT was computed using the following relation:

$$DPAT = DPT_{w,i} - DPT_{d,o} \qquad (16)$$

where $DPT_{d,o}$ and $DPT_{w,i}$ denote the dew point temperatures of dry outlet and wet inlet, respectively.

2.4.2 | Water recovery ratio

The WRR indicates the quantity of diffused water from the wet-side to the dry-side compared to the ideal possible water transfer. Here, WRR was calculated using the following relation[25]:

$$WRR = \frac{\omega_{d,o} - \omega_{d,i}}{\omega_{w,i}} \qquad (17)$$

where ω denotes the humidity ratio (g/g), and the subscripts of d and w represent the dry side and wet side, respectively. The subscripts of i and o indicate the inlet and outlets of the humidifier, respectively. Here, the humidity ratio was computed as following[26]:

$$\omega = \frac{p_w}{p - p_w} \cdot \frac{M_w}{M_a} \qquad (18)$$

where the ratio of M_w/M_a denotes the molecular weight ratio of the water to the air. Here, the partial pressure of water vapor (p_w) and total pressure of air (p) are adopted for computations.

2.4.3 | Pressure drop

The pressure drop due to friction losses was computed as the pressure difference between the average inlet pressure ($P_{d,i}$) and the average outlet pressure ($P_{d,o}$) of the dry air side as:

$$\Delta P = P_{d,i} - P_{d,o} \qquad (19)$$

3 | NUMERICAL METHOD, MESH STUDY, AND CODE VERIFICATION

The Finite Volume Method (FVM), implemented in ANSYS Fluent software, was used to numerically solve

**TABLE 2** The independent test for the three-serpentine channel

Z(m)	$N_x \times N_y \times N_z$		
	$41 \times 500 \times 500$	$61 \times 750 \times 750$	$69 \times 850 \times 850$
0.0245	4.2538	4.1799	4.1846
0.1805	19.4816	18.6079	18.8299
0.2985	22.4189	22.6770	22.8330
0.401	28.0816	28.1921	28.5711
Relative error	3.46%–1.65%	1.32%–0.11%	0%

the governing equations with respect to the imposed boundary conditions. All governing equations were discretized using the second-order upwind scheme.

The SIMPLE algorithm proposed by Patankar[29] was adopted for coupling between the velocity and pressures. The convergence condition for all equations was taken as 10^{-6}. The pressure-velocity coupling relationship is solved by using SIMPLE (Semi-Implicit Method for Pressure-Link Equation). More details about the utilized numerical approach can be followed in References 25, 26. The geometrical and physical details of the flow channels are reported in Table 1. The geometrical specification of the serpentine channels is as follows: $H=H_1 = H_2 = 1$ mm, and $t = 25$ μm.

As a part of the numerical study and ensuring the accuracy of the results, the grid-independent test was performed for various grid sizes, and the results are summarized in Table 2. The four temperature points were adapted along the left flow channel of the three-serpentine channel to monitor the flow temperatures. Here, $Z(m)$ stands for the distance along the flow channel from inlet to monitor point. The grid size of $69 \times 850 \times 850$ was adopted as the reference for computing the relative temperature differences. Table 2 shows that the averaged relative error of $61 \times 750 \times 750$ is about 1.32%–0.11%; hence, this grid was selected for the computations of the present research.

The code verification was performed by comparison of the results with the literature data of Houreh and Afshari[9] for a rectangular humidifier with the geometry of Figure 1A. The simulation was carried out according to the same geometrical and boundary conditions, reported in the literature. The simulation area was a block enclosed by the dotted line, as shown in Figure 1A. The dotted lines are the left and right walls of the simulation area were considered periodic boundary conditions since the humidifier was a multiple flow channel design. The height (1 mm) and width (1 mm) were applied for the wet and dry sides of the humidifier. The channel's length was also fixed as 200 mm with a film thickness of 25 μm. For the boundary conditions, the following were applied: dry air ($\varphi_{d,i} = 0\%$)
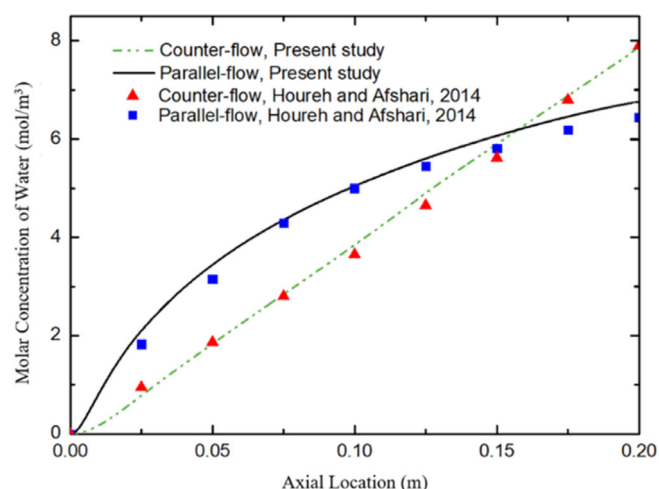
FIGURE 3 A comparison of the change of mass concentration along the dry channel obtained in the present study and those reported by Houreh and Afshari[9] [Colour figure can be viewed at wileyonlinelibrary.com]

with $T_{d,I} = 30°C$ and mass flow rate of $\dot{m}_{d,i} = 9 \times 10^{-6}$ kg/s at the inlet for dry side. For the wet side, an inlet air with a mass flow rate $\dot{m}_{w,i} = 9 \times 10^{-6}$ kg/s, relative humidity $\varphi_{d,i} = 0\%$, and temperature $T_{d,i} = 80°C$ was applied. Figure 3 depicts the variation of water concentration along the channel for two cases of parallel flow and counter flow designs. As seen, the results of both studies are in very good agreement, and the relative error of the simulation results is less than 3%. In the case of parallel flow, the current model slightly overestimates the water concentration near the outlet. The reason for such a difference could be due to the slight change of thermophysical properties, which were considered constant in the present study.

4 | RESULTS AND DISCUSSION

Here, the humidification performance of serpentine flow channels has been investigated for various control parameters to find the best serpentine geometry. Then,

the influence of the dry and wet sides inlet temperature, and airflow mass rate, and the relative humidity on the humidifying behavior of the selected channel will be addressed.

In this section, the impact of the number of flow channels on the performance of the humidifier is examined. The inlet air condition on the dry side was set at 30°C, 60% RH, and the inlet air condition on the wet-side was 70°C and 100%RH. The mass flow rate of the air on the wet-side was 90×10^{-6} kg/s. The temperature and vapor concentration contours on the cross-section of dry side near membrane for the four flow channel designs were compared under the above conditions in Figures 4 and 5.
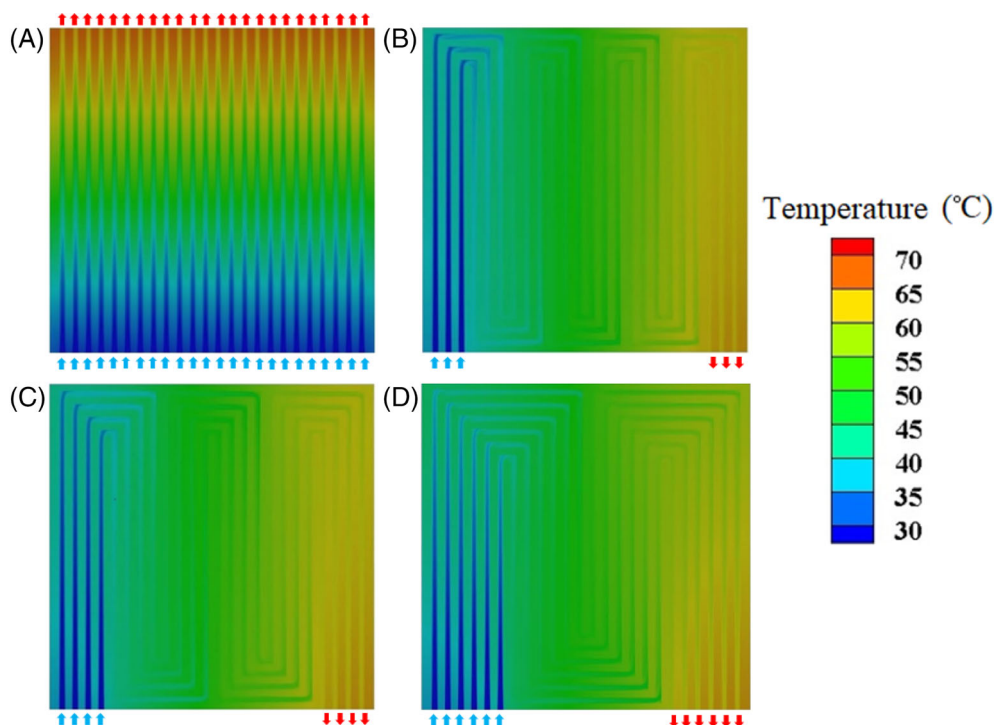
FIGURE 4 The temperature contours on the cross-section of dry side near membrane for various flow channel designs. (A) Straight flow channel, (B) three-serpentine flow channel, (C) four-serpentine flow channel, and (D) six-serpentine flow channel [Colour figure can be viewed at wileyonlinelibrary.com]
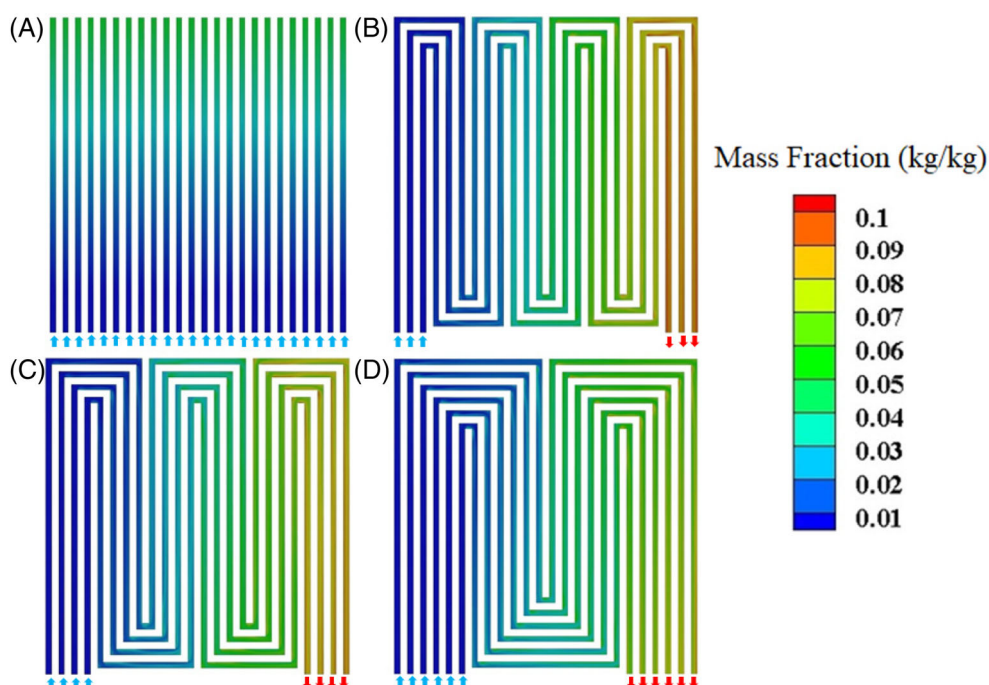
FIGURE 5 The vapor concentration contours on the cross-section of dry side near membrane for various flow channel designs. (A) Straight flow channel, (B) three-serpentine flow channel, (C) four-serpentine flow channel, and (D) six-serpentine flow channel [Colour figure can be viewed at wileyonlinelibrary.com]

—WILEY |

4.1 | Temperature and concentration distributions

As seen in Figure 4A, the temperature distribution of the direct flow channel in the red region is well developed at the outlet compared to the other channels. Hence, the outlet temperature for this design with a temperature of 62.45°C is the highest among the four channels. This figure also shows a developed green area at the outlet of the straight flow channel, indicating poor mass transfer efficiency. The mass transfer of the straight channel is the worst among the four flow channel designs. The shorter the length, the worse the mass transfer performance.

Figure 4B–D shows that the temperature distributions of the three-serpentines, four-serpentines, and six-serpentines designs are almost identical within 1°C. The outlet temperature of the three-serpentine channel design is the lowest among the three designs, so it can

be seen that the number of serpentine passages and the influence of the number of turns on the heat transfer is not significant. The comparison of red concentration regions, next to the outlet area in Figures 5B and 6C,D, illustrates that the outlet of the three serpentines is more developed compared to the other channels. This proper concentration distribution could be due to the longer length of the membrane interface between the dry and wet streams, which effectively contributes to the mass transfer.

Figure 6 shows the temperature and humidity variations along the channel's axis. Figure 6A displays that the straight channel design provides the shortest flow path, but it leads to the highest outlet temperature. In agreement with the graphical outcomes of Figure 6A, this figure shows that all of the serpentines channel designs eventually result in similar outlet temperatures. Figure 6B depicts that the three-serpentines have higher outlet water vapor concentration due to the longer flow channel length. In contrast, in the case of the straight channel, the outlet water vapor concentration is the lowest due to the short length of the channel.

Based on the results of Figures 4-6, it can be concluded that the mass transfer performance of the three-serpentine channel design is the best, while the heat transfer performances are almost identical. Hence, the three-serpentine flow design was adopted as the best geometry for further investigations. In the following subsections, the humidification behavior of the three-serpentine flow channel for various control parameters will be surveyed.
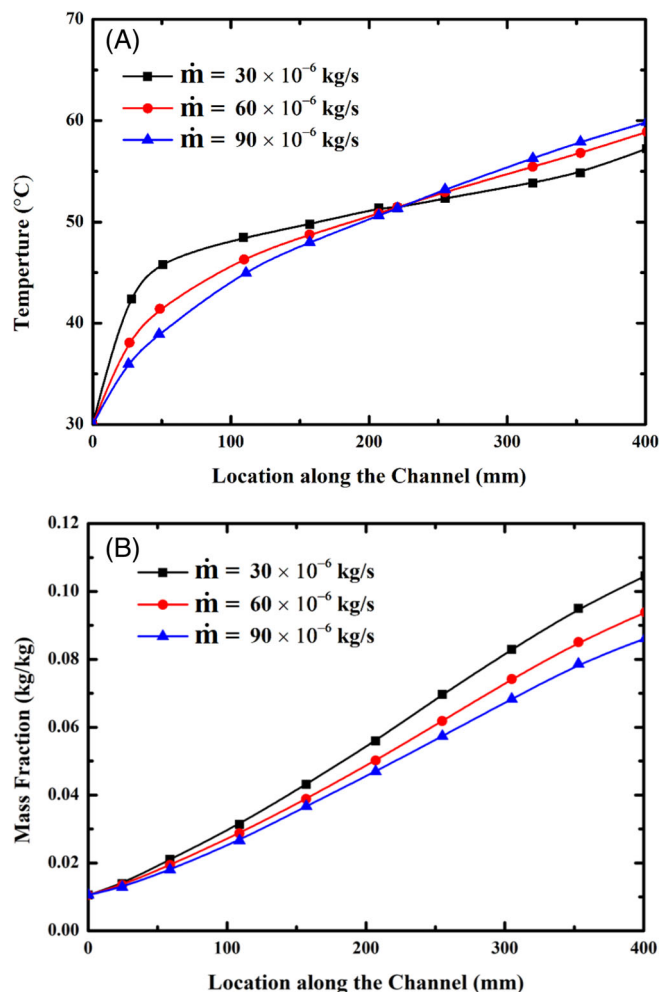
4.2 | Air-mass flow rate

In this section, the three-serpentine flow channel is adopted to study the heat and mass transfer in the humidifier at various inlet mass flow rates. The wet side inlet air condition is fixed at 70°C and 100% RH, and the mass airflow rate on the dry side is equal to the mass airflow rate on the wet-side. The control parameters are the dry side inlet temperature and the inlet mass flow rate. The air mass flow rate at the wet side is fixed the same as the dry side for convenience. The relative humidity of the dry side was fixed at 10%. The temperature and relative humidity at the wet-side were set at 70°C and 100%, respectively.

Figure 7 shows the influence of the mass flow rate on the temperature and concentration variations of the dry flow along the channel. According to previous studies,[25,26] the lower the flow rate, the higher the outlet temperature at the dry side. Moreover, the higher the flow rate, the lower the outlet temperature on the dry
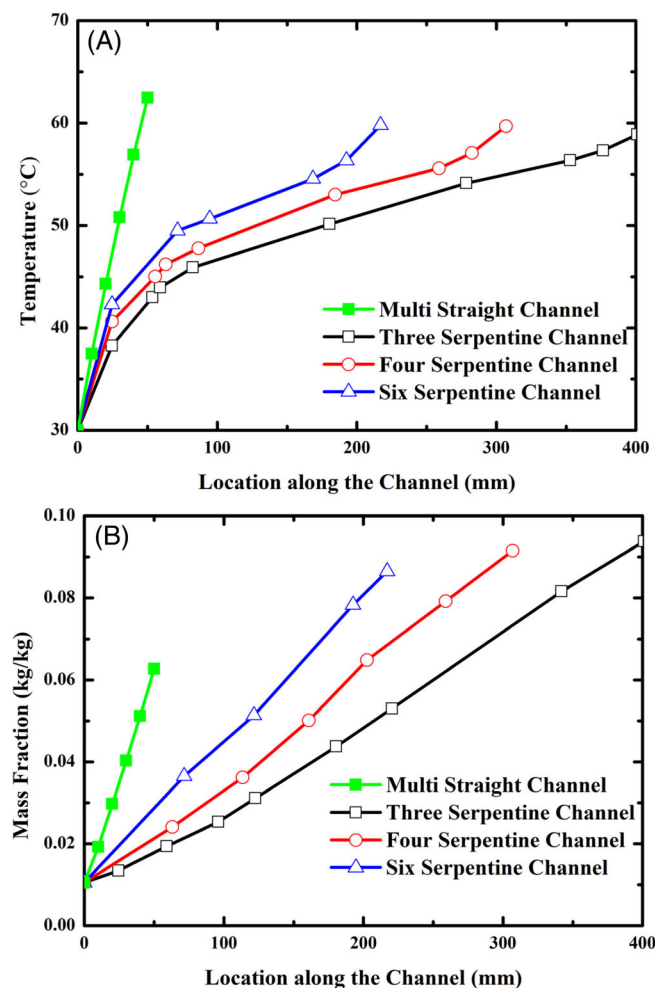
FIGURE 6 Variations of temperature and concentration changes along the channel for various channel designs. (A) Temperature distribution, (B) water concentration [Colour figure can be viewed at wileyonlinelibrary.com]

FIGURE 7 Variations of temperature and concentration changes along the channel axis for various mass flow rates. (A) Temperature variation, (B) concentration variation [Colour figure can be viewed at wileyonlinelibrary.com]

side. However, the result of the serpentine flow channel is entirely the opposite. Figure 7A exhibits the initial dry-side air temperature inclines slowly in the high flow state, but the temperature of the dry-side air gradually increases along the flow direction. When the mass flow rate is high, the heating rate is not suitable at the initial length of the channel. However, at the long distances from the inlet, the temperature rises, and the heat transfer rate from the wet channel to the dry channel improves. Conversely, for a low mass flow rate, the temperature of the dry channel can quickly increase at the initial stages due to the low overall heat capacity of the fluid flow. However, the low heat capacity leads to a weak heat exchange effect in the second half of the flow channel. It can be seen from Figure 7B that the mass transfer is reduced at a high flow rate. These outcomes are consistent with the simulation results in the previous

section. Almost similar results were found for the variation of the mass flow rate of the wet side.

4.3 | Dry-side inlet conditions

Figure 8 shows the influence of the air temperature and water mass flux on the dew point approximate temperature (Figure 8A), WRR (Figure 8B), pressure drop (Figure 8C), and water mass transfer (Figure 8D) at the dry side of the flow channel. Figure 8A displays that the higher the temperature of the dry side air, the lower the dew point of the outlet air. Moreover, the larger the flow rate, the lower the dew point. Figure 8B illustrates that the WRR rises when the dry inlet temperature reduces. Rising the flow rate reduces WRR since the membrane layer imposes a resistance to mass diffusion and limits the mass transfer rate. Figure 8C shows that the growth of temperature slightly inclines the pressure drop. This is since the inlet on the dry side already contains a higher amount of water vapor at 50°C. The density variation leads to the growth of the flow velocity and the raise of the pressure drop at the dry channel. Figure 8D displays that the lower the dry air temperature, the lower the water flux. An increase in the flow rate leads to higher water flux since a high flow rate improves the total amount of water at the membrane layer. Moreover, it should be noted that although the increase of mass flow rate boosts the total water flux, the accumulated water should be distributed in a much larger amount for the dry flow. So, humidity may be decreased despite the increase in the total water flux.

As a summary, the increase of temperature at the dry-side reduces the DPAT, WRR, and water flux, while it inclines pressure drop. Moreover, the increase of flow rate reduces the DPAT and WRR while raises pressure drop and water flux.

4.4 | Wet-side inlet conditions

Here, the impacts of the inlet air temperature at the wet-side and the flow rate (at the dry and wet-sides) are examined on the characteristics parameters of the humidifier. The variables are the wet-side inlet temperature and the inlet mass flow rates. The mass flow rates at the wet and dry sized were set similar for convenience. The wet-side inlet condition was 100%, while the dry-side inlet air condition was fixed at 30°C and 60%RH. According to the above set of control parameters, DPAT, WRR, pressure drop, and water flux were computed and plotted in Figure 9. Figure 9A exhibits the DPAT as a function of the mass flow rate. As seen, the lower the temperature on
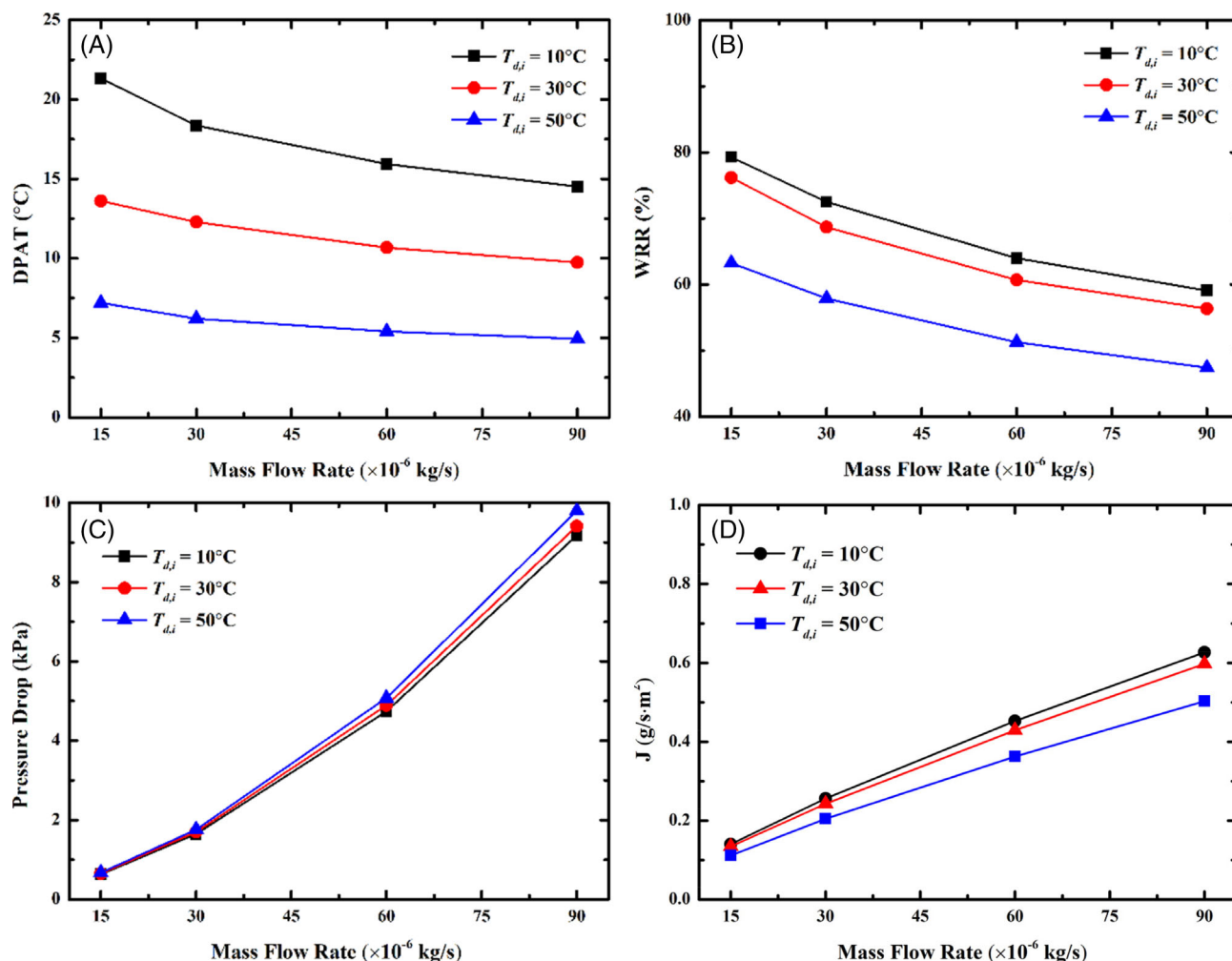
FIGURE 8 Effects of the dry-side inlet air temperature and mass flow rate. (A) Dew point approach temperature, (B) water recovery ratio, (C) pressure drop, and (D) water flux [Colour figure can be viewed at wileyonlinelibrary.com]

the wet-side, the lower the DPAT. Figure 9B shows that the increase of temperature enhances the WRR since the gas with a higher temperature could carry a higher volume of moisture. So, the diffusion between the dry and wet sides raises, which consequently improves the water vapor transfer rate. However, when the mass flow rate increases, the gas leaves the channel faster, and the actual time span of mass transfer diminishes. Hence, the higher the mass flow rate, the lower the WRR.

Figure 9C displays that the raise of the temperature slightly increases the pressure drop. This is since an increase in the temperature inclines the mass diffusion and, consequently, the momentum transfer. The fluids at the dry and wet channels move in opposite directions, so any mass transfer with opposite momentum would lead to a significant pressure drop. Figure 9C also shows that the increase in the mass flow rate leads to a drastic rise in the pressure drop due to the friction effects. Figure 9D shows that the increase in the temperature would raise

the water flux due to the improvement of mass diffusion. Although the relative humidity of each temperature is 100%, the rise of the temperature boosts the amount of water vapor in the saturated air. So, a larger amount of water can be diffused to a high-temperature air at the dry side.

The impact of the relative humidity of the inlet air at the wet-side on the characteristic parameters of the humidifier was also investigated. The wet-side temperature was set at 70°C, and the inlet temperature and relative humidity at the dry-side were fixed at 30°C and 60%, respectively. The mass airflow rate on the dry side was set equal to the mass airflow rate on the wet side. The control parameters were the relative humidity and mass flow rate. It was found that the increase of the relative humidity results in a slightly lower DPAT, but it enhances the WRR. Moreover, the higher the relative humidity, the richer the air mixture, and consequently, the higher the diffusion rate from the wetside to the dry-
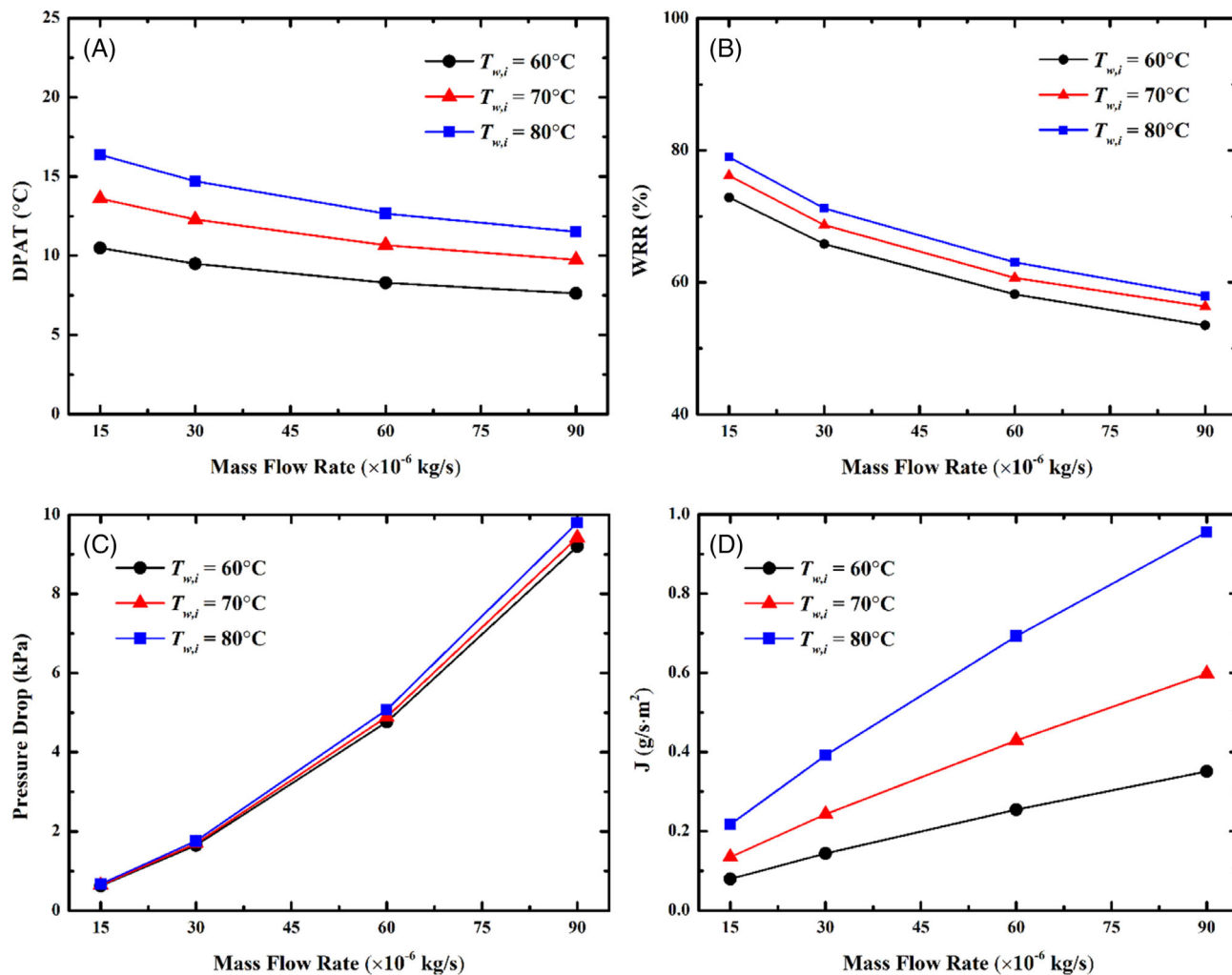
FIGURE 9 Effects of the wet-side inlet air temperature and mass flow rate. (A) Dew point approach temperature, (B) water recovery ratio, (C) pressure drop, and (D) water flux [Colour figure can be viewed at wileyonlinelibrary.com]

side. Indeed, the concentration difference in the humidity of wet and dry sides is a significant driving force for mass transfer through the membrane. It also observed that change of relative humidity has minimal impact on the pressure drop. The study[33] also reported that changing the relative humidity at the dry side has no effect on the performance of the humidifier.

5 | CONCLUSIONS

In the present research, a model of humidifier consisting of a thin membrane humidifier was used to analyze the heat and mass transfer in between wet and dry channels. Various geometries of the humidifier, including straight flow channels, and three-, four-, and six- serpentine flow channels, were examined. The three-serpentine flow channel was selected as the best geometry configuration for best

humidification and a reasonable heat transfer rate with a slight increase in pressure drop. The main outcomes of the present study can be summarized as follows:

1. Increasing the dry-side temperature reduces DAPT and WRR, while it slightly increases the pressure drop. The increase of mass flow rate reduces DAPT and WRR, while it increases the pressure drop and water flux. Hence, a rise in the inlet temperature of the dry channel deteriorates the humidifier functions and should be avoided.
2. Increasing the wet side temperature enhances the DPAT, and improves WRR and the water flux, but it also slightly increases the pressure drop. Hence, the higher the wet side temperature, the better humidification.
3. The rise of the wet-side relative humidity improves the WRR and the water flux with minimal impact on

the pressure drop and DPAT. Thus, keeping the inlet humidity of the wet-side as high as possible is always beneficial, but its benefit is not much.

4. The number of channels induces a minimal effect on the heat transfer, but the variation of the mass transfer is significant. The three-serpentine channel has the largest area, and therefore, has the highest water vapor transmission effect.

ACKNOWLEDGEMENT

DATA AVAILABILITY STATEMENT

Data is contained within the article.

ORCID

Bing-Bing Wang https://orcid.org/0000-0002-2377-053X
Wen-Ken Li https://orcid.org/0000-0001-8835-701X
Mohammad Ghalambaz https://orcid.org/0000-0003-0965-2358

REFERENCES

1. Wilberforce T, Ijaodola O, Khatib F, et al. Effect of humidification of reactive gases on the performance of a proton exchange membrane fuel cell. *Sci Total Environ*. 2019;688:1016-1035.
2. Zhang Q, Tong Z, Tong S. Effect of cathode recirculation on high potential limitation and self-humidification of hydrogen fuel cell system. *J Power Sources*. 2020;468:228388.
3. Sanchez DG, Ruiu T, Biswas I, Schulze M, Helmly S, Friedrich KA. Local impact of humidification on degradation in polymer electrolyte fuel cells. *J Power Sources*. 2017;352:42-55.
4. Casalegno A, De Antonellis S, Colombo L, Rinaldi F. Design of an innovative enthalpy wheel based humidification system for polymer electrolyte fuel cell. *Int J Hydrogen Energy*. 2011;36(8):5000-5009.
5. Cha D, Yang W, Kim Y. Performance improvement of self-humidifying PEM fuel cells using water injection at various start-up conditions. *Energy*. 2019;183:514-524.
6. Ahmaditaba AH, Afshari E, Asghari S. An experimental study on the bubble humidification method of polymer electrolyte membrane fuel cells. *Energy Sources A*. 2018;40(12):1508-1519.
7. Govindan PN, Thiel GP, McGovern RK, Lienhard JH, Elsharqawy MH. Humidification-dehumidification system with a bubble-column vapor mixture condenser and intermediate gas extraction. Google Patents; 2016.
8. Shao Y, Xu L, Zhao X, et al. Comparison of self-humidification effect on polymer electrolyte membrane fuel cell with anodic and cathodic exhaust gas recirculation. *Int J Hydrogen Energy*. 2020;45(4):3108-3122.
9. Houreh NB, Afshari E. Three-dimensional CFD modeling of a planar membrane humidifier for PEM fuel cell systems. *Int J Hydrogen Energy*. 2014;39(27):14969-14979.

10. Firouzjaei VK, Rahgoshay S, Khorshidian M. Planar membrane humidifier for fuel cell application: numerical and experimental case study. *Int J Heat Mass Transf*. 2020;147:118872.
11. Chang Y, Qin Y, Yin Y, Zhang J, Li X. Humidification strategy for polymer electrolyte membrane fuel cells–a review. *Appl Energy*. 2018;230:643-662.
12. Lucas C, Staeck R. Humidifier having an integrated water separator for a fuel cell system, fuel cell system and vehicle comprising same. Google Patents; 2018.
13. Lucas C, Staeck R. Humidifier with an integrated water separator for a fuel cell system, fuel cell system including a humidifier, and vehicle including same. Google Patents; 2017.
14. Noh YG, Kim HY. Humidifier for fuel cell system. Google Patents; 2018.
15. Becker M, Hoefler T, Wimmer H. Membrane humidifier, preferably for a fuel cell system. Google Patents; 2019.
16. Fuelcellstore. Fuel Cell Stack Humidifier—5kW; 2020. https://www.fuelcellstore.com/fuel-cell-stack-humidifier-5000w.
17. Chen C-Y, Yan W-M, Lai C-N, Su J-H. Heat and mass transfer of a planar membrane humidifier for proton exchange membrane fuel cell. *Int J Heat Mass Transf*. 2017;109:601-608.
18. Yan W-M, Chen C-Y, Y-k J, Chang Y-H, Amani P, Amani M. Performance evaluation of a multi-stage plate-type membrane humidifier for proton exchange membrane fuel cell. *Energ Conver Manage*. 2018;176:123-130.
19. Atyabi SA, Afshari E, Jamalabadi MYA. Three-dimensional multiphase flow modeling of membrane humidifier for PEM fuel cell application. *Int J Numer Methods Heat Fluid Flow*. 2019;30:54-74.
20. Solsona M, Kunusch C, Ocampo-Martinez C. Control-oriented model of a membrane humidifier for fuel cell applications. *Energ Conver Manage*. 2017;137:121-129.
21. Afshari E, Baharlou HN. An analytic model of membrane humidifier for proton exchange membrane fuel cell. *Energy Equip Syst*. 2014;2(1):83-94.
22. Kong IM, Jung A, Kim MS. Investigations on the double gas diffusion backing layer for performance improvement of self-humidified proton exchange membrane fuel cells. *Appl Energy*. 2016;176:149-156.
23. Chen C-Y, Su J-H, Ali HM, Yan W-M, Amani M. Effect of channel structure on the performance of a planar membrane humidifier for proton exchange membrane fuel cell. *Int J Heat Mass Transf*. 2020;163:120522.
24. Afshari E, Houreh NB. Performance analysis of a membrane humidifier containing porous metal foam as flow distributor in a PEM fuel cell system. *Energ Conver Manage*. 2014;88:612-621.
25. Yan W-M, Lee C-Y, Li C-H, Li W-K, Rashidi S. Study on heat and mass transfer of a planar membrane humidifier for PEM fuel cell. *Int J Heat Mass Transf*. 2020;152:119538.
26. Yan W-M, Li C-H, Lee C-Y, Rashidi S, Li W-K. Numerical study on heat and mass transfer performance of the planar membrane-based humidifier for PEMFC. *Int J Heat Mass Transf*. 2020;157:119918.
27. Nield DA, Bejan A. Heat transfer through a porous medium. *Convection in Porous Media*. New York, USA: Springer; 2017:37-55.
28. Wang Y, Wang C-Y. Simulation of flow and transport phenomena in a polymer electrolyte fuel cell under low-humidity operation. *J Power Sources*. 2005;147(1–2):148-161.

29. Motupally S, Becker AJ, Weidner JW. Diffusion of water in Nafion 115 membranes. *J Electrochem Soc*. 2000;147(9): 3171.

30. Chen D, Peng H. A thermodynamic model of membrane humidifiers for PEM fuel cell humidification control; 2005.

31. Gurau V, Liu H, Kakac S. Two-dimensional model for proton exchange membrane fuel cells. *AIChE J*. 1998;44(11): 2410-2422.

32. Bejan A. *Convection Heat Transfer*. Hoboken, USA: John Wiley & Sons; 2013.

33. Houreh NB, Afshari E. An analytic and numerical modeling of a membrane humidifier for PEM fuel cell. Paper presented at: 6th Iranian Fuel Cell Seminar; March 12–13, 2013; Tehran, Iran: Shahid Rajaee Teacher Training University.